Growth kinetics and morphology of snowflakes in supersaturated atmosphere using a three-dimensional phase-field model

G. Demange,[1] H. Zapolsky,[1] R. Patte,[1] and M. Brunel[2]

[1]*GPM, UMR CNRS 6643, University of Rouen, 76575 Saint Étienne du Rouvray, France*

[2]*CORIA UMR 6614, University of Rouen, 76575 Saint Étienne du Rouvray, France*

Simulating ice crystal growth is a major issue for meteorology and aircraft safety. Yet, very few models currently succeed in reproducing correctly the diversity of snow crystal forms, and link the model parameters to thermodynamic quantities. Here, we demonstrate that the new three-dimensional phase-field model developed in Demange *et al.* [npj Comput. Mater. **3**, 1 (2017)] is capable of reproducing properly the morphology and growth kinetics of snowflakes in supersaturated atmosphere. Aside from that, we show that the growth dynamics of snow crystals satisfies the selection theory, consistently with previous experimental observations. Finally, we link the parameters of the phase-field model to atmospheric parameters.

I. INTRODUCTION

The formation process of snowflakes keeps challenging the scientific community [1] as the growth mechanism remains yet misunderstood [2]. Indeed, snowflake morphology at millimetric scale results from the interplay of complex phenomena, from quantum mechanics at a atomic scale [3], to facet kinetics at a macroscopic scale. Beyond theoretical consideration, ice crystal morphology has also piqued interest of industrials. Notably, meteorology and aircraft safety require the development of metrologies such as interferometric imaging [4,5], to estimate ice water content in clouds. The calibration of such devices relies upon the preliminary compilation of realistically simulated snowflakes and the dependence of their morphology on atmospheric conditions.

The study of snowflake morphology was addressed experimentally first. In a pioneering work, Nakaya observed that the vapor-ice phase transition resulted in a wide manifold of patterns and sizes of snowflakes [6]. The systematic indexation of snowflake morphologies to temperature and humidity resulted in the most famous Nakaya diagram [7]. More recent meteorological classifications can also be found in other studies [8–10]. In spite of the vast amount of experimental data, the physics behind ice crystal growth remains thoroughly debatable [11]. Even now, various models are still being considered, such as the *layer nucleation rates* [12] and the *quasiliquid layer* [13].

Alternatively, the first step toward the understanding of ice crystal growth was provided by molecular dynamic simulations [14]. However, these studies are currently confined to space and time scales several orders of magnitude smaller than the characteristic scales of snowflake growth [10]. Then, the cellular automaton model was used to reproduce several snowflake morphologies [15–18]. Yet, this model is very sensitive to numerous numerical parameters, sometimes hard to relate to thermodynamics quantities. This shortcoming was withal relieved in Ref. [17]. Nevertheless, it is not perfectly clear how additional physical mechanisms can be added to the procedure. For instance, introducing fluid dynamics might be required to simulate the impact of air flow on the morphology of snowflakes.

Continuous models are promising to palliate the shortcomings of cellular automata. Among such, the sharp interface model of Barrett *et al.* [19] succeeded in simulating various snowflake morphologies. However, this method could not account for characteristic snowflake features in three dimensions, such as side branching [20], surface markings [21,22], and snow crystal aggregation [23]. Aside from that, only small supersaturations could be prospected, due to the numerical cost of interface parametrization [24]. Now, the phase-field model [25–28] has the decisive advantage to overcome the explicit tracking of the sharp boundary, by spreading out the interface over a small layer, and reduce the computation load of simulations. And yet, it was only with Barret *et al.* in Ref. [29] first, and Demange *et al.* [30] more recently, that the phase-field approach succeeded in simulating the growth of snow crystals in three dimensions.

In Ref. [31], the growth process of simulated snowflakes was assumed to result from the synergistic effect of a highly anisotropic surface tension, and a kinetic attachment vertical anisotropy [31]. A major hypothesis in this model was to free itself from the constraint of the slow growth regime [32]. The challenge of this work is to investigate if under these hypotheses, the model is capable of simulating the formation of snowflakes, while preserving a consistent growth process and realistic morphologies. The underlying objective is to provide experimentalists with a reliable and versatile numerical tool that predicts snowflake growth and morphology in supersaturated atmosphere. To our knowledge, this was never achieved before.

This work is structured as follows. First, an overview of the phase-field model developed in Ref. [30] is provided. It is accompanied by the regularization procedure for the highly anisotropic surface tension. Second, the numerical growth process of simulated snowflakes is studied in the fast and slow growth directions. Then, the growth kinetics of simulated ice dendrites is confronted to the solvability theory. Finally, the simulations are linked to experiments by the intermediate of a morphology diagram of snowflakes.

II. OVERVIEW OF THE PHASE-FIELD MODEL

1. Kinetic equations

The kinetics is described by an order parameter ϕ referring to the ice $(+1)$ and vapor (-1) phases, and the

reduced supersaturation of water vapor $u = (c - c_{\text{sat}}^I)/c_{\text{sat}}^I$. Here, $c_{\text{sat}}^I(T)$ is the saturation number density of vapor above ice, at temperature T. At initial time, the reduced supersaturation u_0 is homogeneous. The growth kinetics of snowflakes is governed by two nonconservative phase-field equations:

$$A(\boldsymbol{n})^2 \partial_t \phi = -f'(\phi) + \lambda B(\boldsymbol{n}) g'(\phi) u$$
$$+ \frac{1}{2} \boldsymbol{\nabla}_\Gamma \cdot \left\{ |\boldsymbol{\nabla}_\Gamma \phi|^2 \frac{\partial [A(\boldsymbol{n})^2]}{\partial \boldsymbol{\nabla} \phi} + A(\boldsymbol{n})^2 \boldsymbol{\nabla}_\Gamma \phi \right\} \quad (1)$$

$$\partial_t u = \widetilde{D} \boldsymbol{\nabla}_\Gamma \cdot [q(\phi) \boldsymbol{\nabla}_\Gamma] u - \frac{L_{\text{sat}}}{2} B(\boldsymbol{n}) \partial_t \phi, \quad (2)$$

where space and time are scaled by the ice-vapor interface width W_0 and the relaxation time of the interface propagation τ_0, respectively. In Eq. (1), the double well potential $f(\phi) = -\phi^2/2 + \phi^4/4$ is the free energy density of the ice-vapor system, at temperature T, and saturation concentration $c = c_{\text{sat}}^I$. $g'(\phi) = (1 - \phi^2)^2$ is an interpolation function introduced in Ref. [25]. λ is a numerical coupling parameter. The first source of anisotropy $B(\boldsymbol{n}) = (n_x^2 + n_y^2 + \Gamma^2 n_z^2)^{1/2}$ is a kinetic anisotropy function accounting for different water molecule attachment rates on the basal and prismatic faces of snowflakes [32], where $\boldsymbol{n} = -\boldsymbol{\nabla}\phi/|\boldsymbol{\nabla}\phi|$ is the unit normal vector of ϕ. In $B(\boldsymbol{n})$, the parameter $\Gamma > 0$ governs the preference between horizontal ($\Gamma < 1$) and vertical ($\Gamma > 1$) growth. The second source of anisotropy $A(\boldsymbol{n}) = 1 + \epsilon_{xy} \cos(6\theta) + \epsilon_z \cos(2\psi)$ is the surface tension anisotropy function. Here, ϵ_{xy} and ϵ_z are the anisotropy constants, and θ and ψ are the polar and azimuthal angles of the contour normal vector $\boldsymbol{n}$, defined by $\theta = \arctan[n_y/n_x]$ and $\psi = \arctan[(n_x^2 + n_y^2)^{1/2}/n_z]$. $A(\boldsymbol{n})$ accounts for the only common symmetries to most snowflake morphologies. These are the horizontal sixfold symmetry and the vertical planar symmetry. To mimic faceting in the horizontal plane or in the vertical direction, one of the anisotropy constants ϵ_{xy} or ϵ_z must be chosen so that the equilibrium crystal shape (ECS) associated to $A(\boldsymbol{n})$ displays missing orientations. It should be noted that it is technically possible to impose the symmetry of the crystal, as well as faceting, by the intermediate of a purely kinetic anisotropy, as it is the case in Ref. [33]. However, we believe that the sixfold hexagonal symmetry of snowflakes cannot be explained by kinetic effects, but only by surface tension anisotropy (even weak), inherited from the crystal structure of ice. In Eq. (2), $q(\phi) = 1 - \phi$ prohibits diffusion within ice. $\widetilde{D}$ is the reduced diffusion coefficient. L_{sat} is the depletion rate of water molecules in vapor, due to ice phase growth. Finally, the vertical scaling of interfaces is introduced via anisotropic space derivative $\boldsymbol{\nabla}_\Gamma = (\partial_x, \partial_y, \Gamma \partial_z)$, which reduces the interface width in the slow growth direction. The constants λ, W_0, τ_0, and $\widetilde{D}$ are entangled with each other by the thin interface limit approach [25,26]: $W_0 = d_0 \lambda/a_1$, $\widetilde{D} = a_2 \lambda$, where d_0 is the isotropic capillarity length, $a_1 = 0.8839$, and $a_2 = 0.6267$ [27]. Besides, the anisotropic interface width $W_0 A(\boldsymbol{n})$ is linked to the characteristic time of interface propagation $\tau_0 A(\boldsymbol{n})^2$, where $\tau_0 = a_2 \lambda W_0^2$.

2. Simulation method

1. Highly anisotropic surface tension

In this work, snowflake facets were mimicked by rounded faces with a large radius of curvature. This can be achieved by providing the surface tension anisotropy function $A(\boldsymbol{n})$ with high energy directions, which generate unstable orientations in the equilibrium shape of the crystal (ECS) [34]. These unstable orientations correspond to sharp corners in the ECS, pairing with the nonconvexity of the parametric plot of $1/A(\boldsymbol{n})$. For these orientations, the phase field [Eq. (1)] becomes ill posed, and $A(\boldsymbol{n})$ must be regularized. In this work, we supposed that unstable orientations were produced either in the vicinity of the vertical direction (ψ close to 0 and π) or in the vicinity of six equiangular horizontal directions for θ. This hypothesis allowed us to use the two-dimensional (2D) regularization algorithm of Eggleston *et al.* [35,36] in three dimensions, either for the θ variable or for the ψ variable. The principle is as follows. In two dimensions, the reduced anisotropy function $A(\boldsymbol{n})$ reduces to $A(\theta)$. Unstable crystal orientation is simply characterized by a negative stiffness $A + \partial_{\theta\theta}^2 A < 0$ [37], when the anisotropy constant ϵ reaches a threshold value ϵ^m. However, this formalism is not valid for higher dimensions in the general case [38]. That being said, considering that the two variables θ and ϕ of $A(\theta, \psi)$ are decoupled, such criterion can be transposed to three dimensions, provided only one of the anisotropy constants ϵ_{xy} or ϵ_z reaches its threshold value ϵ_{xy}^m or ϵ_z^m. This threshold value is defined as the minimum value of ϵ_{xy} (resp. ϵ_z), for which the equation $A + \partial_{\theta\theta}^2 A = 0$ (resp. $A + \partial_{\psi\psi}^2 A = 0$) admits solutions. ϵ_{xy}^m and ϵ_z^m follow:

$$\epsilon_{xy}^m = \frac{1 + \epsilon_z \cos(2\psi)}{35}, \quad \epsilon_z^m = \frac{1 + \epsilon_{xy} \cos(6\theta)}{3}. \quad (3)$$

Considering this set of equations, regularizing the missing orientations in three dimensions raises two issues. First, ϵ_{xy}^m and ϵ_z^m depend on ψ and θ, respectively. Second, ϵ_{xy}^m and ϵ_z^m are entangled with ϵ_z and ϵ_{xy}. Consequently, raising the horizontal hexagonal anisotropy ϵ_{xy} also enlarges the range of missing orientations in the vertical direction, and vice versa.

Invoking the rotation periodicity of $A(\theta, \psi)$, we restrict the procedure to $\theta \in [-\pi/6, \pi/6]$ and $\psi \in [0, \pi]$. When ϵ_{xy} or ϵ_z is locally superior to $\epsilon_{xy}^m(\psi)$ or $\epsilon_z^m(\theta)$, missing orientations (θ, ψ) emerge, within a certain angular sector $[-\theta^m, \theta^m]$ or $[-\psi^m, \psi^m]$ [see Figs. 1(a) and 1(b)]. The bounds θ^m and ψ^m can be detected by a local inversion of the convexity of $1/A(\boldsymbol{n})$. For each coordinate, the concave part of the curve is determined by the tangent construction of Eggleston *et al.* [35]. Following this procedure, θ^m and ψ^m, respectively, satisfy the following conditions: $\partial_\theta [\cos(\theta)/A(\theta, \psi)]|_{\theta=\theta^m} = 0$ and $\partial_\psi [\cos(\psi)/A(\theta, \psi)]|_{\psi=\psi^m} = 0$. This provides the following implicit definition of θ^m and ψ^m:

$$\frac{6\epsilon_{xy} \sin(6\theta^m)}{\sin(\theta^m)} = \frac{1 + \epsilon_{xy} \cos(6\theta^m) + \epsilon_z \cos(2\psi)}{\cos(\theta^m)},$$
$$\frac{2\epsilon_z \sin(2\psi^m)}{\sin(\psi^m)} = \frac{1 + \epsilon_{xy} \cos(6\theta) + \epsilon_z \cos(2\psi^m)}{\cos(\psi^m)}. \quad (4)$$

This set of equations shows that $\theta^m = \theta^m(\psi)$ and $\psi^m = \psi^m(\theta)$. Now, missing orientations are identified and can be
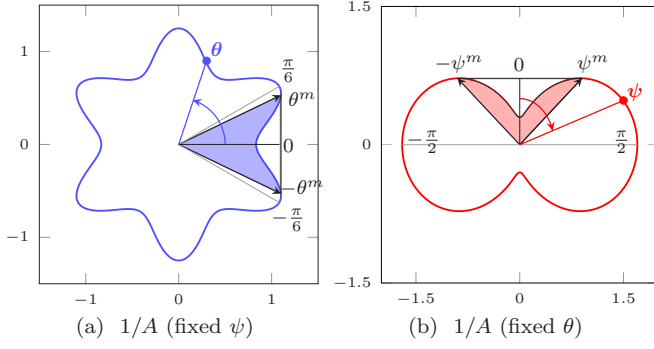
(a) $1/A$ (fixed ψ)   (b) $1/A$ (fixed θ)

FIG. 1. Inverse plot of the anisotropy function $A(\boldsymbol{n})$, for $\epsilon_{xy} = 0.2$ and $\epsilon_z = 0.7$. Top left: $1/A(\theta,\pi/4)$, limit angle $\theta^m(\pi/4)$, and tangent construction between θ^m and $-\theta^m$. Top right: $1/A(\pi/12,\psi)$, limit angle $\psi^m(\pi/12)$, and tangent construction between ψ^m and $-\psi^m$.

regularized. For that purpose, $A(\boldsymbol{n})$ must be continuously spliced in the corresponding directions. In this work, $A(\theta,\psi)$ was prolonged by a trigonometric function:

$$A(\theta,\psi) = \begin{cases} A_1 + B_1 \cos(\theta), & |\theta| < \theta^m, |\psi| \geqslant \psi^m \\ A_2 + B_2 \cos(\psi), & |\theta| \geqslant \theta^m, |\psi| < \psi^m \\ 1 + \epsilon_{xy} \cos(6\theta) + \epsilon_z \cos(2\psi), & \text{otherwise.} \end{cases}$$

(5)

In Eq. (5), the functions A_1, A_2, B_1, and B_2 are set to ensure continuity of $A(\boldsymbol{n})$ and its derivatives:

$$A_1(\psi) = 1 + \epsilon_{xy} \cos(6\theta^m) + \epsilon_z \cos(2\psi) - B_1 \cos(\theta^m),$$

$$B_1(\psi) = \frac{6\epsilon_{xy} \sin(6\theta^m)}{\sin(\theta^m)},$$

$$A_2(\theta) = 1 + \epsilon_{xy} \cos(6\theta) + \epsilon_z \cos(2\psi^m) - B_2 \cos(\psi^m),$$

$$B_2(\theta) = \frac{2\epsilon_z \sin(2\psi^m)}{\sin(\psi^m)}.$$

(6)

The result of the regularization procedure is summarized in Fig. 2, in case of unstable orientations along horizontal directions ($\epsilon_{xy} = 0.1 > \epsilon_{xy}^m$ and $\epsilon_z = 0.3 < \epsilon_z^m$) and along the vertical direction ($\epsilon_{xy} = 0.02 < \epsilon_{xy}^m$ and $\epsilon_z = 0.6 > \epsilon_z^m$). Before regularization, the 2D Wulff shape (WS) for the ECS displays "ears" corresponding to unstable orientations [Figs. 2(a)–2(c)]. The associated inverse 2D polar plot is concave in these directions [inside blue curve in Figs. 2(j)–2(l)]. After regularization, the ears are removed [Figs. 2(d)–2(f)], and the inverse polar plot becomes convex [outside red curve in Figs. 2(j)–2(l)]. Aside from that, the resulting 2D polar plot is regular and coincides with the original 2D polar plot where the curvature was already positive before the regularization procedure [red curve in Figs. 2(g)–2(i)].

2. Numerical scheme

To model the growth of ice crystals, Eqs. (1) and (2) were solved in three dimensions, using a semi-implicit time integration. Besides, the Fourier collocation treatment of space was used [39]. This allows to get rid of the second order derivatives, thus achieving faster computation. The correct estimation of the angles θ and ϕ that appear in $A(\boldsymbol{n})$ required to use directional derivatives. Indeed, centered derivatives dramatically raise the truncation error, when $\boldsymbol{n}$ is aligned with

(a) WS ($\psi = \frac{\pi}{2}$)   (b) WS ($\psi = \frac{\pi}{4}$)   (c) WS ($\theta = 0$)

(d) ECS ($\psi = \frac{\pi}{2}$)   (e) ECS ($\psi = \frac{\pi}{4}$)   (f) ECS ($\theta = 0$)

(g) A ($\psi = \frac{\pi}{2}$)   (h) A ($\psi = \frac{\pi}{4}$)   (i) A ($\theta = 0$)

(j) $1/A$ ($\psi = \frac{\pi}{2}$)   (k) $1/A$ ($\psi = \frac{\pi}{4}$)   (l) $1/A$ ($\theta = 0$)
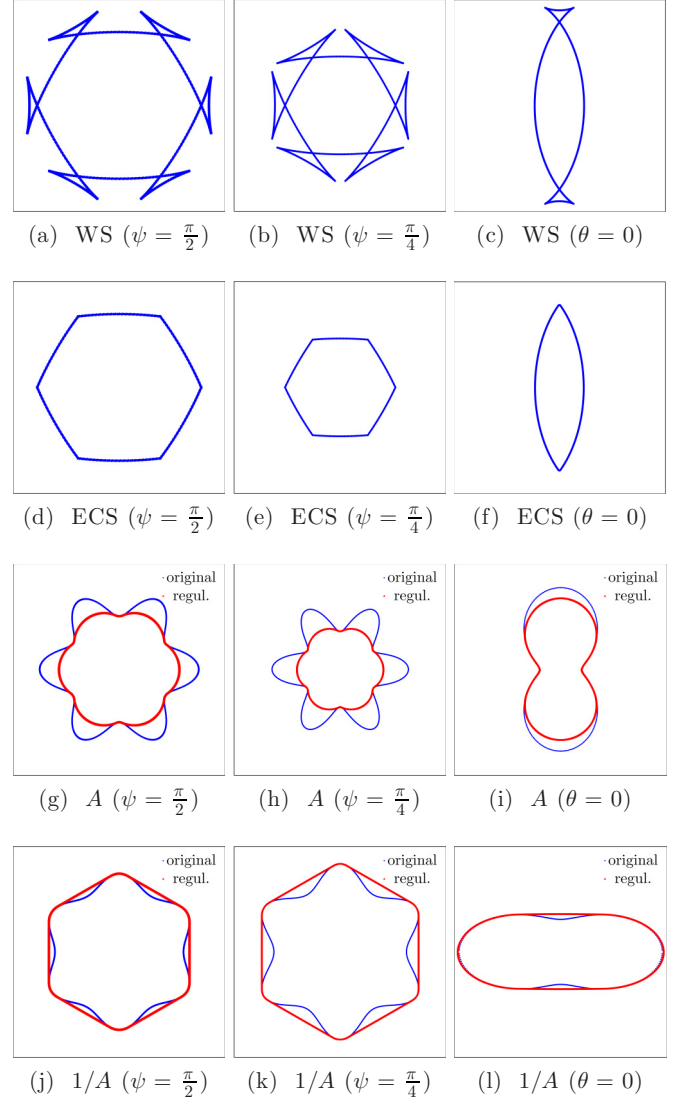
FIG. 2. 2D Wulff construction in the horizontal plane for $\epsilon_{xy} = 0.1$ and $\epsilon_z = 0.3$ in $\psi = \pi/2$ (a) and $\psi = \pi/4$ (b), and in the vertical direction for $\epsilon_{xy} = 0.02$ and $\epsilon_z = 0.6$, in $\theta = 0$. (d)–(f) Corresponding ECS after regularization. (g)–(i) Corresponding polar plot before (outside curve in blue), and after (inside curve in red) regularization. (j)–(l) Corresponding inverse polar plot before (inside curve in blue), and after (outside curve in red) regularization.

the grid. This discrepancy is amplified near the front most tip of the dendrite, in case of highly anisotropic surface tension [35]. This issue is crucial, as the dendrite tip velocity sets the size of the dendrite. In the present case of sixfold symmetry, all branches cannot benefit from equal precision. This can lead to a symmetry breaking, and even snowflake instability. Hence, decentered derivatives were used within a fixed angular sector centered in (Ox), (Oy), and (Oz), where grid effects are the strongest. The decentering direction was the same as the phase flux [35]. Remaining derivatives were centered. Finally, periodic boundary conditions were used.

3. Parameter setting

For horizontal growth, simulations were performed using the grid spacing $\Delta x = \Delta y = \Delta z = 0.8$, and the time step

$\Delta t = 0.05$ [27], on a $400 \times 400 \times 64$ simulation box ($800 \times 800 \times 96$ for * in Fig. 13). Vertical growth simulations required a refined discretization grid. The grid spacing was thus reduced to $\Delta x = \Delta y = \Delta z = 0.4$, and the time step was set to $\Delta t = 0.01$, as in Ref. [27], on a $128 \times 128 \times 256$ simulation box. The growth of snowflakes was initiated by a circular-disk shape germ ($\phi = 1$), within water vapor ($\phi = -1$) of homogeneous reduced supersaturation u_0. The simulation germ cannot be assimilated to the nanoscopic nucleus of experimental snowflakes, as such nucleus is by several orders of magnitude smaller than the characteristic space scale of phase field. However, it can be seen as the early stage of real snowflake grown in supersaturated atmosphere [40]. In this work, we opted for a circular disk germ rather than a sphere because it accelerates the formation of flat snowflakes in case of horizontal growth. The disk germ radius was set to $8\Delta x$. The coupling constant was set to $\lambda = 3.0$ as in Ref. [27]. Other parameters are given in Ref. [30].

III. RESULTS

A. Snowflake growth process

In this model, the growth process rooting the morphology of snowflakes results from the joint influence of the vertical kinetic anisotropy $B(\boldsymbol{n})$ and the highly anisotropic surface tension $A(\boldsymbol{n})$. The vertical anisotropy contribution sets a slow and a fast growing direction, leading to planar or columnar morphologies. The surface tension is responsible for the hexagonal symmetry, the faceted aspect of the crystal in the horizontal plane, and the twofold symmetry in the vertical direction [30].

1. Surface tension and branching instability in the fast growth direction

In the fast growing direction, two processes compete: the highly anisotropic surface tension and the branching instability. The highly anisotropic surface tension is responsible for the horizontal hexagonal symmetry and vertical twofold symmetry, and the faceted aspect of the simulated crystal. As for the branching instability, it relates to the Berg effect, stating that the supersaturation field around a crystal remains regular [41]. For instance, the crystal displays sharp edges in Fig. 3(b), but the supersaturation level set $u = 0.3$ is very smooth (black lines). As a consequence, the supersaturation is largest at edges ($u \simeq 0.25$) and weakest at face centers ($u \simeq 0$). A divergent feedback process of vapor diffusion eventually increases the growth rate in the vicinity of corners. At some point, the difference of supersaturation between edges and face centers becomes too large to be offset by surface tension anisotropy. The velocity eventually becomes smaller at the face center, and the facet breaks.

The competing effect of the highly anisotropic surface tension and the branching instability is responsible for the formation of primary branches. In the horizontal direction first [Fig. 3(a)], the effect of the surface tension predominates when the crystal is small ($t \leqslant 50$). The shape of the snow crystal thus aligns on the hexagonal ECS associated to the anisotropic surface energy function $A(\boldsymbol{n})$. Above some critical crystal radius ($t \sim 50$), the branching instability occurs, and

(a) Horizontal growth
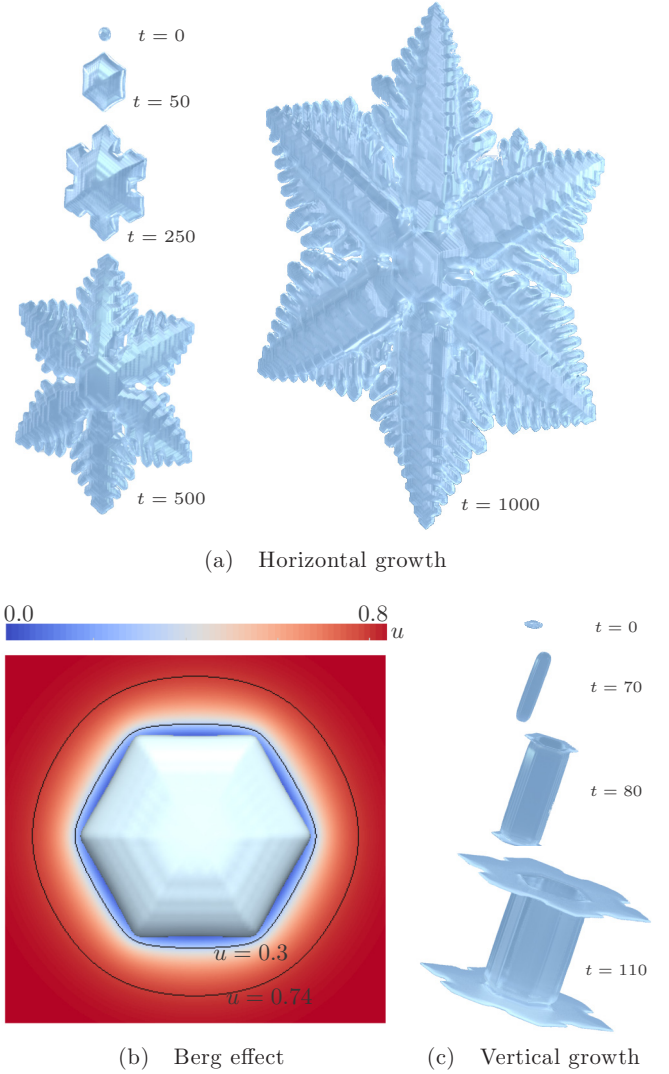

(b) Berg effect   (c) Vertical growth

FIG. 3. Growth process of simulated snowflakes. (a) Contour representation ($\phi = 0$) of a fern dendrite growth. (b) Early growth of a fern dendrite and supersaturation field u. (c) Contour representation ($\phi = 0$) of a capped column growth. Time in τ_0 units. Visual rendering uses the software Blender.

horizontal dendrites are formed. In some cases of horizontal growth, the branching instability is horizontal, resulting in a "sandwich instability" [16], as observed in Ref. [42]. When the growth is vertical, the branching instability is involved in the formation of a curved tip on column snowflakes, and the formation of a hollow on the basal faces of prisms [30]. The branching instability is also involved in the formation of caps in Fig. 3(c), when the atmospheric conditions are changed during the growth.

The competing effect of the highly anisotropic surface tension and the branching instability is also responsible for side branching. In our simulations, the side branching process is qualitatively similar to that of experimental ice crystals with a faceted tip (see Fig. 5 in Ref. [43]). As can be seen in Fig. 4, the corner of the primary branch (black circle) is prominent. It thus undergoes the divergent feedback process described above. Meanwhile, a new primary branch emerges from the
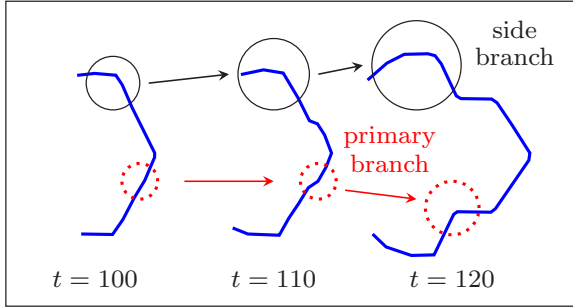
FIG. 4. Side branching process for highly anisotropic surface tension. The simulations correspond to the fern dendrite. Time is in τ_0 unit.

(a) Sectored plate   (b) Stellar dendrite

FIG. 6. Principal growth stages of (a) a sectored plate and (b) a stellar dendrite. Blue line: real snowflake from [46]. Red circles: phase-field simulation [30]. 1,2,3: growth stages.

initial primary branch (red dashed circle). As such, the red dashed circle in the simulation process indicates the formation of "concaves" on real faceted ice crystals [43]. Finally, the original corner of the primary branch (black circle) becomes the nucleus for a side branch. The present mechanism for side branching results from the highly anisotropic surface tension, which leads to the formation of sufficiently sharp corners on the sides of the primary branch. Therefore, it differs from the side branching process in case of weakly anisotropic surface tension, stemming from infinitesimal fluctuations of supersaturation or temperature in the vicinity of the dendrite tip [44].

In a nutshell, the kinetics of real snowflake growth in air is phenomenologically reproduced in the fast growth direction. However, the mechanism of faceting which is suspected to result from the slow growth limits in real snowflakes [45] is mimicked in our simulations by the effect of a highly anisotropic surface tension in the horizontal plane. The consequence of this choice on the dendrite tip velocity is addressed in the following.

2. Kinetic anisotropy and terrace growth in the slow growth direction

In the slow growth direction, solid-vapor interactions are strongly reduced, due to the kinetic anisotropy function $B(\boldsymbol{n})$. The first consequence is the quasi-impossibility for the branching instability to take place. However, the growth is slow, but not stopped. It produces terraces, separated by "macrosteps," also simulated in Refs. [16,17]. These can be seen in Fig. 5. Similar surface patterns were observed on experimental snowflakes by the intermediate of interference fringes [22].
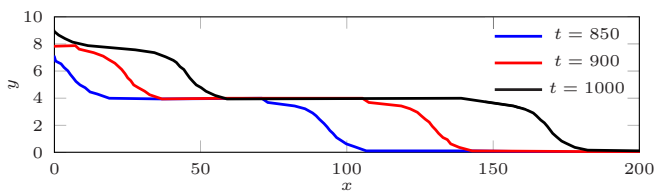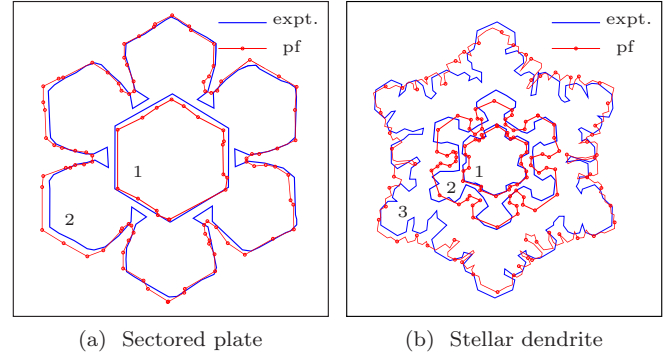

FIG. 5. Terrace growth and terrace-step-kink propagation in our simulations. The simulations correspond to the sectored plate. Time is in τ_0 unit. The interface width is close to 3.

In details, the terrace is perpendicular to the slow growth direction. The terrace-step kink moves outward as it is plotted in the surface cut of Fig. 5. The propagation mechanism of the step is the following: the water molecule attachment in the direction normal to the terrace is strongly reduced because of the kinetic anisotropy function $B(\boldsymbol{n})$. Thus, water molecule attachment is effective at the step only. Moreover, the diffuse interface is scaled by Γ in the slow growth direction, so that the vapor-ice interface thickness is reduced. As a result, the surface of the terrace is phenomenologically smooth, while the surface of the step is phenomenologically rough. This description of macrosteps is similar to the model of branch growth in Ref. [47]. At a completely different space scale, this growth process is reminiscent of the formation of 2D islands on the surface of ice facets [21]. Nonetheless, this comparison is qualitative only, as molecular attachment processes at atomic scale are not addressed by the phase-field model.

The macrosteps that are produced by brutal transitions in the growth process, such as the branching instability, are particularly well defined. We thus suggest that the succession of flat basal planes on both real and simulated snowflakes reflects the main stages of the snowflake growth history. This idea was previously formulated in Ref. [47]. Figure 6 compares the main stages of growth, between the real snowflake (blue line) and the simulation (red line and circles) for the sectored plate [Fig. 6(a)] and the stellar dendrite [Fig. 6(b)]. In the case of the sectored plate [Fig. 6], the system keeps memory of the solid hexagonal plate (stage 1) before the branching instability appears (stage 2). In that case, experimental and numerical results are in good agreement. Besides, both transient solid plates have a similar size, relative to the size of the snowflake. This suggests that the branching instability occurred at the same stage of their development. This observation indicates that the present model reproduces well the real phenomenon. This is even more striking with the stellar dendrite [Fig. 6(b)]. Here, three growth stages (1, 2, and 3) can be identified. Once again, the three corresponding basal steps match between the real snowflake and the simulation. The first step is the vestige of a solid plate. During the second step, six small sectors are formed. The last step consists of the dendrite growth.
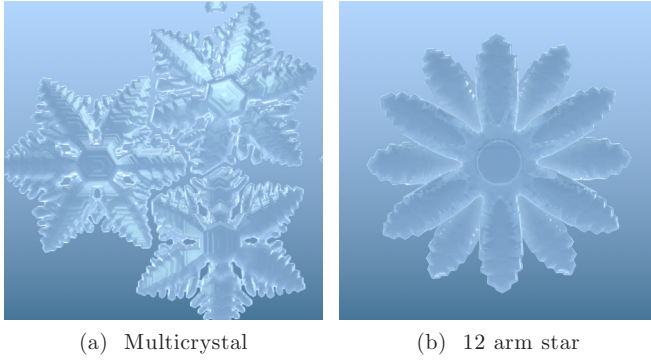
(a) Multicrystal (b) 12 arm star

FIG. 7. Simulation of the simultaneous growth of multiple snowflakes. (a) Three fern dendrite snowflakes grow simultaneously in the plane. (b) 12 arm star. Surface plot uses the software Blender for visual rendering.

3. Multiple seed growth process

Under certain atmospheric conditions, snowflakes aggregate and form clusters [48]. The phase-field model developed in Ref. [30] was thus provided with the multiple seed growth procedure developed in Ref. [49]. In this approach, each snowflake grows from a different seed, with a specific orientation defined by a tilt angle θ_0 in the anisotropy function $A(\mathbf{n})$. Two examples of multiple seed growth are presented in Fig. 7.

First, Fig. 7(a) shows the planar growth of three fern dendrite snowflakes. Each snowflake is characterized by a different tilt angle: $\theta_0 = 0$ (bottom), $\theta_0 = \pi/12$ (top), and $\theta_0 = \pi/6$ (left). It can be observed that the growth is perturbed when snow crystals are too close from each other. The neighboring branches are abnormally packed, and they are deprived from side branching. This stems from the local decrease in supersaturation between snowflakes, and consequently the chemical driving force. When the supersaturation goes to 0, the growth is blocked. This observation is consistent with experimental data in Ref. [49]. A second example is provided by the 12 arm star in Fig. 7(b). In that case, two seeds grow in parallel, until it aggregates at their basal faces. It was observed in Ref. [23] that the two coalescing halves of the 12 arm star are tilted by a 30° angle in nature. In our simulation, this tilt angle was imposed to one of the two halves.

B. Parabolic growth and solvability theory for simulated snowflakes

1. Ivantsov framework for ice needles and dendrites

The dendrite tip model of Ivantsov [50] provides a useful analytical framework to study the growth kinetics of dendrites. At the root of it, the approximation of the dendrite tip by a revolution paraboloid. In both our simulations (4) and experiments (3), needles are nearly axisymmetric. Aside from that, the longitudinal cut of the needle tip can reliably be fitted ($\rho > 0.99$) by a parabola of parameter R. This is displayed in the inset of Fig. 8(b) for the simulated needle (red circles).

On the contrary, ice horizontal dendrites are not cylindrically symmetric [see Fig. 3(a)]. However, a link with analytical models can be made, when the morphology of the ice dendrite
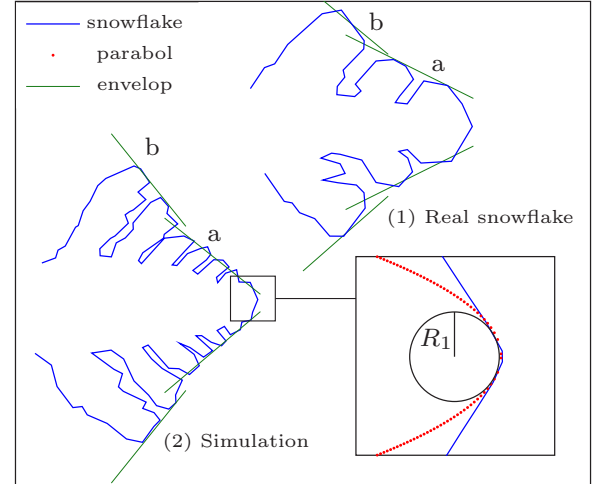
(a) Dendrite top shape
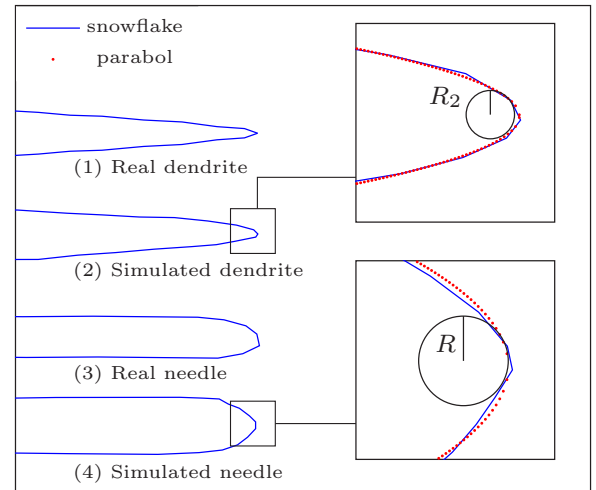
(b) Dendrite profile shape

FIG. 8. Tip morphology of a fern dendrite. (a) Contour representation (blue line) of a fern dendrite in the horizontal direction, from experimental (1) snowflakes [22,46] and our simulations (2). Inset: zoom on the dendrite front most tip. (b) Fern dendrites (1) and (2) in the vertical direction, and column snowflake from experimental (3) snowflakes [46] and our simulations (4). Red circles: Ivantsov parabola fit of dendrite tip. Green line: envelope for side branching.

is considered separately in the horizontal [Fig. 8(a)] and vertical planes [Fig. 8(b)]. Here, the contour of the simulated stellar dendrite from [30] is compared to the real snowflake from [46] (top view) and [22] (profile view).

In the horizontal direction [Fig. 8(a)], despite the sharp and faceted shape of the dendrite, the front most tip [inset in Fig. 8(a)] remains curved, and can also be fitted by a parabola of parameter R_1. This procedure is physically acceptable, as snow crystals growing in highly supersaturated atmosphere display a round tip as well [43]. However, the curved area of the simulated dendrite tip is small. This generates an uncertainty on the estimation of R_1, resulting in an important dispersion of measures. In the vertical direction [Fig. 8(b)], albeit extremely sharp, the simulated dendrite tip (1) can reliably be fitted by a parabola of parameter R_2 (red circles in the top right inset). As
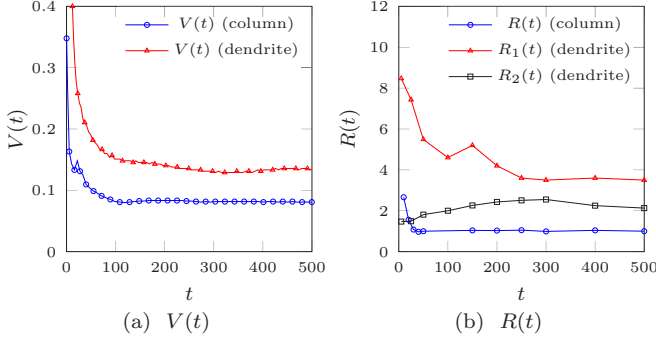
(a) $V(t)$ (b) $R(t)$

FIG. 9. Time evolution of the tip velocity V and tip curvature radii R, for the column growth (blue circle) and the fern dendrite in the horizontal (red triangle) and vertical (black square) directions. Vertical growth: $u_0 = 0.4$. Horizontal growth: $u_0 = 0.65$.

a result, the three-dimensional (3D) tip shape of ice horizontal dendrites can be modeled by two parabola: horizontal of radius R_1 and vertical of radius R_2. From R_1 and R_2, it is also possible to define the geometric mean radius $\sqrt{R_1 R_2}$ of a virtual cylindric paraboloid [51]. A more accurate description of the situation would be provided by the elliptical paraboloid model of Horvay and Cahn [52]. However, this approach is beyond the scope of this work, and is left to a future study.

In passing, the side branching morphology is also characterized in Fig. 8(a). In particular, the linear envelope (green lines) for side branches [18] is recovered. In the region neighboring the dendrite tip (a), the growth rate of young side branches is small because branches restrain each other. At some point, "winning" side branches are selected, and the growth rate is increased (b). As a result, the slope of the linear envelope is changed.

2. Ivantsov solution, stability theory, and universal law

The time evolution of the dimensionless dendrite tip velocity $V(t)$ and curvature radius $R(t)$ are shown in Figs. 9(a) and 9(b). Here, R was defined by the intermediate of the parabola fitting of the dendrite tip introduced in Fig. 8. The simulations were performed with $u_0 = 0.4$ for the vertical growth (blue circles) and $u_0 = 0.65$ for the horizontal growth. For the latest, the curvature radius in the horizontal direction R_1 (red triangle) and in the vertical direction R_2 (black square) were studied. It can be seen that after a short transition regime ($t \leqslant 100$), $V(t)$ and $R(t)$ become stationary. This is consistent with the *steady-state* theory for dendrite growth [50]. This framework was originally defined for a nearly paraboloid tip growing at constant velocity without change in shape, but it is also satisfied experimentally by nonaxisymmetric and faceted dendrite growth, especially snowflakes [32]. It should be noted that the fluctuations of $R_1(t)$ most likely result from the uncertainty of the curvature radius estimation. This is due to the small sector of the horizontal dendrite where the front most tip is curved [see Fig. 8(a)].

The steady-state values of $V(t)$ and $R(t)$ are written V^s and R^s for a given supersaturation u_0. In the case of the horizontal ice dendrite, R^s may refer to R_1^s, R_2^s, or $\sqrt{R_1^s R_2^s}$. Repeating the same procedure for different values of u_0, the evolution of V^s and R^s with u_0 could be plotted in Figs. 10(a)

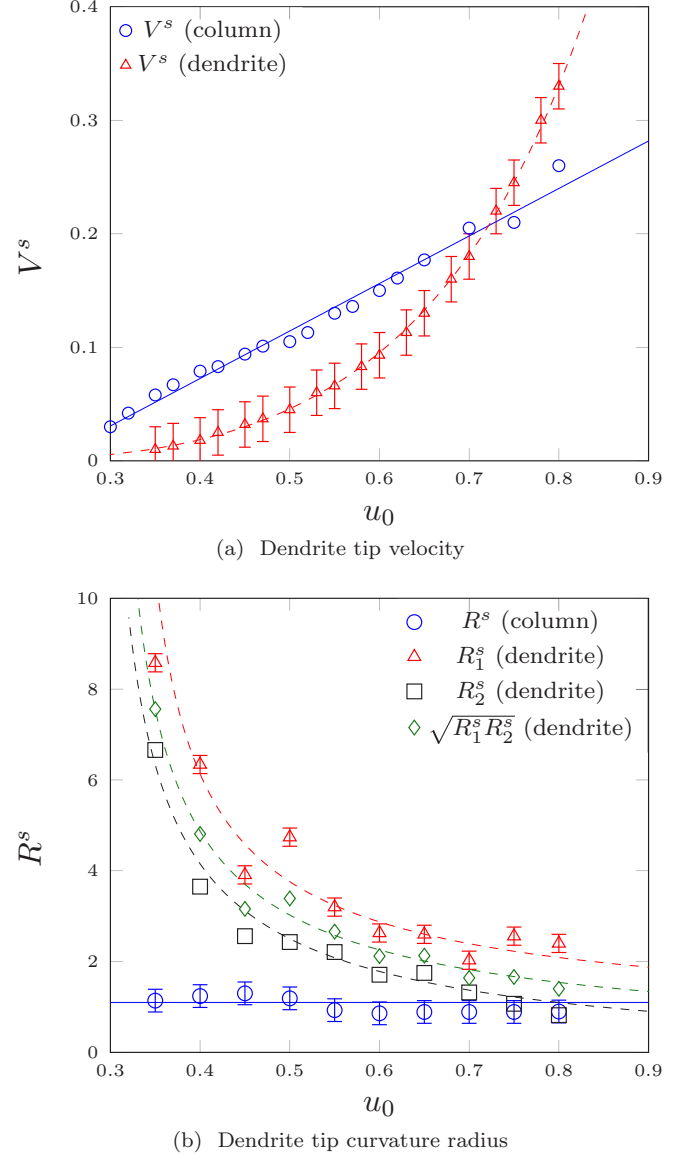(a) Dendrite tip velocity

(b) Dendrite tip curvature radius

FIG. 10. Steady-state values V^s and R^s of the tip velocity and tip curvature radii, as a function of the supersaturation u_0, for the column growth (blue circle) and the fern dendrite in the horizontal (red triangle) and vertical (black square) directions. Green diamond in (b): geometric mean radius $\sqrt{R_1^s R_2^s}$. Continuous line: linear fit. Dashed line: regression based on Ivantsov solution and the stability theory (each curve differs from the other by a translation only).

and 10(b). For the needle growth (blue circle), the relation between V^s and u_0 is linear, with a slope 0.42 [blue line in Fig. 10(a)]. Moreover, R^s is stable [blue line in Fig. 10(b)]. This relation between V^s and u_0 was experimentally observed during needle dendrite growth in supersaturated atmosphere [53]. For the horizontal dendrite growth, it was suggested in [30] that the relation was linear as well for low to intermediate supersaturations ($u_0 \leqslant 0.55$). This is indeed consistent with the data on this range of supersaturations, with a slope 0.22 (red line). Besides, a linear relation was also observed in Ref. [19] for $u_0 \leqslant 0.5$. However, when one considers the complete range of tested supersaturations ($0.3 \leqslant u_0 \leqslant 0.8$), the relation between the tip velocity and the supersaturation
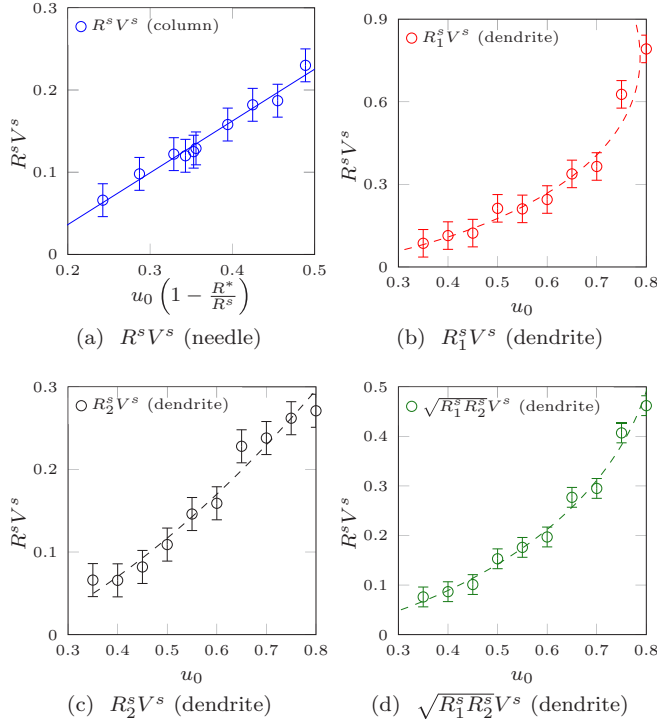
FIG. 11. Relation between $R^s V^s$ and u_0 based on 3D Ivantsov solution, for the needle (a), the horizontal curvature radius of the dendrite (b), and the vertical curvature radius of the dendrite (c), and the geometric mean (d) radius. Straight line in (a): linear regression. Dashed line in (b)–(d): fitting with Ivantsov solution.

rather satisfies the universal law adapted from [54], following [51]: $u_0 \sim -\alpha\sqrt{V^s}\ln[\alpha\sqrt{V^s}]$ [red dashes in Fig. 10(a)], where $\alpha = [a_1/(2\tilde{D}\lambda s^*)]^{1/2}$ (fitting value $\alpha = 0.17$). Here, the constant s^* is the stability parameter. Moreover, contrary to the needle tip, R_1^s (red triangle), R_2^s (black square), and $\sqrt{R_1^s R_2^s}$ (green diamond) decrease, in accordance with the relation adapted from [54]: $u_0 \sim -\gamma/R^s \ln[\gamma/R^s]$ (dashes), where $\gamma = a_1/(\lambda s^*)$ (fitting value $\gamma = 0.09$).

The behavior of both needle and horizontal dendrite kinetics can be discussed in the framework of the solvability theory [55,56]. First, the Ivantsov's solution [50] relates a product $V^s R^s$ to the supersaturation u_∞, far from the dendrite tip. In this work, the simulation box was sufficiently big to ensure the condition $u_\infty = u_0$. The following approximation of the unmodified Ivantsov formula can thus be derived for small values of u_0 [51]:

$$u_0 = -\frac{V^s R^s}{2\tilde{D}} \ln\left[\frac{V^s R^s}{2\tilde{D}}\right]. \tag{7}$$

This relation is numerically satisfied by $V^s R_1^s$ [Fig. 11(b)], $V^s R_2^s$ [Fig. 11(b)], and $V^s \sqrt{R_1^s R_2^s}$ [Fig. 11(b)] products, to a multiplicative constant.

The second relation is the selection of a unique (R^s, V^s) couple, by the intermediate of an additional length scale in the growth kinetics [44]. This length scale is necessary to produce dendrites that grow stably with a constant velocity and tip radius. It can be provided by capillary effects or kinetic anisotropy. When the additional length scale is set by surface
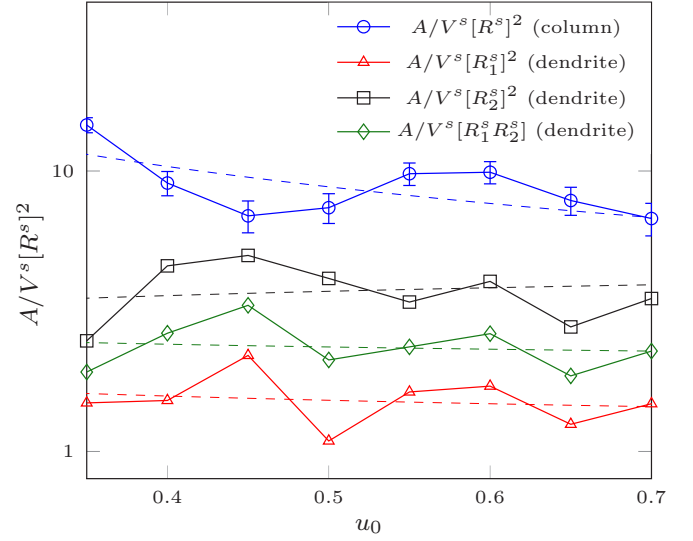

FIG. 12. Steady-state stability parameter $A/(V^s[R^s]^2)$, as a function of the supersaturation u_0, for the column growth (blue circle), and the fern dendrite using the horizontal (red triangle), the vertical (black square), and the geometric mean curvature radius (green diamond). Dashed line: power law regression.

tension, the "marginal stability hypothesis" [44] provides the following stability criterion:

$$\frac{A}{V^s[R^s]^2} = s^*, \tag{8}$$

where the stability parameter s^* is essentially a constant term with respect to extrinsic variables, and $A = 2a_1\tilde{D}/\lambda$. As can be seen in Fig. 12, the quantities $A/(V^s[R_1^s]^2)$, $A/(V^s[R_2^s]^2)$, and $A/(V^s[R_1^s R_2^s])$ remain roughly constant when u_0 varies. Equation (8) is hence satisfied by all (R_1^s, V^s) (red triangle), (R_2^s, V^s) (black square), and $(\sqrt{R_1^s R_2^s}, V^s)$ (green diamond) couples, but with different values for the stability parameter s^*. These are, respectively, $s_1^* = 1.7$, $s_2^* = 4.3$, and $s_{12}^* = 2.7$. Combining Eqs. (7) and (8) provides the universal laws for V^s and R^s, used to fit the numerical results in Fig. 10. Noteworthy, the fitting value for α in Fig. 10(a) is $\alpha = 0.17$. Now, $\alpha = [a_1/(2\tilde{D}\lambda s^*)]^{1/2} = 0.28/\sqrt{s^*}$, so that the expected numerical value for s^* is $s^* = 2.9$, which is close to the numerical value we obtained for the couple $(\sqrt{R_1^s R_2^s}, V^s)$: $s_{12}^* = 2.7$. Notwithstanding, this good consistency should be taken with caution. Indeed, numerical results for V^s, R_1^s, and R_2^s also match the 2D version of Ivantsov solutionbrk $V^s R^s = 2\tilde{D}/\pi u_0^2$, so that V^s increases as $u_0^4/(\pi\alpha)^2$, and R_1^s and R_2^s roughly decrease as $\pi\gamma/u_0^2$, consistently with the predictions of Brener and Melnikov [57,58] for zero kinetic effects in two dimensions.

When capillary effects are negligible compared to the kinetic anisotropy, Libbrecht showed [53,59,60] that the unperturbed Ivantsov solution could be approximated by

$$V^s R^s = A u_\infty \left[1 - \frac{R^*}{R^s}\right]. \tag{9}$$

For the needle growth, Eq. (9) is numerically satisfied in Fig. 9(a), as $V^s R^s$ depends linearly on $u_0(1 - R^*/R^s)$. Here, the linear fit was obtained for $R^* = 0.35$ (straight line).

Besides, when the selection of the dendrite tip radius is governed by attachment kinetics, the stability criterion becomes [32,61]

$$\frac{A'}{V^s[R^s]^2} = \frac{r^*}{u_\infty}, \tag{10}$$

where r^* is another stability parameter, and $A' = 2R^*\tilde{D}$. In the case of needle ice crystals growing in supersaturated atmosphere, $\sigma^s = A'/(V^s[R^s])^2$ was plotted versus u_0 (blue circle) in Fig. 12. Despite the dispersion of the results of simulations, the tendency is consistent with Eq. (10), as $\sigma^s \sim u_0^{-\alpha}$, with $\alpha = 0.85 \pm 0.15$ (blue dashes). Combining Eqs. (9) and (10) imposes that V^s should increase linearly with the supersaturation u_0. Moreover, the tip radius R^s should be independent on u_0. This is in agreement with our observation of V^s and R^s for the needle growth simulation in Fig. 10.

Several remarks can be formulated here. First, this work was performed in the framework of diffusion limited growth. As proof, the Péclet number $P_e^s = R^s V^s/(2\tilde{D})$ is comprised between 0.01 and 0.1 in our simulations. This means that the vapor field adapts very fast to the growth of the snowflake. Moreover, the diffusion length $\ell_{\text{diff}}^s = 2\tilde{D}/V^s$ is always at least one order of magnitude bigger than the curvature radii of the snowflake. However, the present range of Péclet numbers is several orders of magnitude superior to that of real snowflakes in supersaturated atmosphere ($P_e^s \sim 10^{-7}$–10^{-5}), and the slow growth limit for snowflakes is not reached. As it was discussed before, faceting in the dominant growth direction thus cannot result from kinetic effects in the present model, and a highly anisotropic surface tension was required in the model [30]. This explains why the horizontal dendrite tip velocity follows a roughly quartic law in the supersaturation. This is compatible with other phase-field studies using a highly anisotropic surface tension, such as [36].

Second, in the case of needle growth, it is intriguing that the (R^s, V^s) couple satisfies the stability criterion in Eq. (10) for dendrite growth governed by kinetic effects. Indeed, Eqs. (1) and (2) were obtained by canceling the kinetic coefficient β, that is present in the Stefan problem. This allowed to identify the anisotropic time scale $\tau(\boldsymbol{n})$ to the anisotropic space scale $W(\boldsymbol{n})$, consistently with the thin interface limit [25,26]. However, a strong kinetic anisotropy was reintroduced *ad hoc* in Eqs. (1) and (2) by the intermediate of the function $B(\boldsymbol{n})$ and the kinetic parameter Γ, in order to limit the attachment of water molecules in the slow growth direction. Considering that capillary effects are very weak in the needle tip vicinity ($\epsilon_z = 0.01$), we suggest that the growth of the needle is driven by the kinetic anisotropy. Hence, the introduction of $B(\boldsymbol{n})$ in Eqs. (1) and (2) might be responsible for the linear dependence of V^s on u_0, and the validity of Eqs. (9) and (10).

Regarding the solvability theory, an important result is the dependence of the stability parameter s^* on the stiffness parameter ϵ. It was notably demonstrated [62,63] that s^* increases as $\epsilon^{7/4}$, for $\epsilon, P_e \ll 1$. This result was extended to arbitrary Péclet numbers and rapid solidification thereafter [64,65]. However, these studies originally focused on crystals having the fourfold symmetry. It was only recently [51] that the solvability theory was adapted to the underlying sixfold symmetry of snowflake morphology. This general framework remains qualitatively valid for a high stiffness [66],
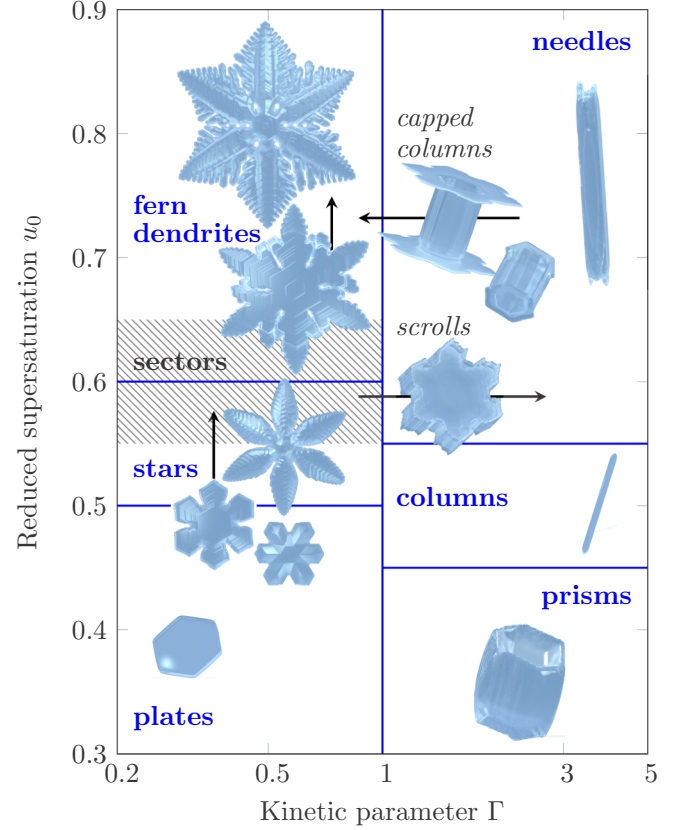

FIG. 13. Γ-u_0 morphology diagram for simulated snowflakes.

consistently with our numerical observations, but it seems that no explicit relation between s^* and ϵ can be found in that case.

Finally, the solvability theory as it was developed in Ref. [63] assumes that the diffusion is symmetric between solid (S) and vapor (V) phases. In this work, the situation is different. Water molecules stay still in ice, and the diffusion is one sided. Conveniently, an extension of the 3D solvability theory for nonsymmetric diffusion can be found in Ref. [66]. In this work, the stability criterion in Eq. (8) was proved to remain valid for one-sided diffusion, but with a different stability parameter $s^* = 2s_{\text{sym}}^*$, where s_{sym}^* is the stability parameter in the symmetric diffusion case. This latest relation was already derived analytically for the 2D growth of needle crystals in [67], after it was observed numerically in Ref. [68].

C. Link with experiments

1. Morphology diagram in reduced units for snowflakes

The morphology of simulated snowflakes results from the interplay of surface tension and kinetic attachment by the intermediate of three principal parameters: Γ, u_0, and L_{sat}. In particular, the variation of the parameters Γ and u_0 allows to sketch the morphology diagram of snowflakes in the kinetic parameter Γ-reduced supersaturation u_0 plane. It is displayed in Fig. 13.

The kinetic parameter Γ yields the attachment efficiency of water molecules on the snowflake surface, in the horizontal and vertical directions. Thus, it determines the "primary habit" in our model [see Fig. 14(a)]. $\Gamma < 1$ produces flat snowflakes
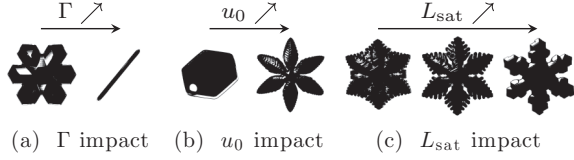
FIG. 14. Schematic representation of the main parameter impact on snowflake morphology.

in the left column of Fig. 13, while $\Gamma \geqslant 1$ gives columnar morphologies in the right column. In our simulations, the primary habit switch was achieved by shifting Γ during growth. This change accounts for the change of temperature in atmosphere due to storms or snowflake fall during growth [16]. This switch of primary habit is represented by a horizontal arrow in Fig. 13.

The parameter u_0 controls the intensity of the thermodynamic driving force. Thus, lower values favor facetlike faces, while higher values facilitate the branching instability [see Fig. 14(b)]. When $\Gamma < 1$, no facet breaking is observed for $u_0 = 0.4$ (bottom left of the morphology diagram). Rising supersaturation near $u_0 = 0.5$ produces a branching instability (middle of Fig. 13). Side branching on dendrites requires $u_0 \geqslant 0.7$. This corresponds to the top-left domain in the morphology diagram. For $\Gamma > 1$, $u_0 = 0.3$ provides a prism (bottom right). Rising u_0 to 0.5 induces the branching instability (column at the middle right). For the highest values of u_0, a hollow is formed at the tip (top right).

The parameter L_{sat} is the depletion rate of vapor induced by the snowflake growth. It sets the amount of water molecules that dendrites consume to grow. Thus, the greater L_{sat}, the less water remains on the side of the dendrites for side branches to grow, and the less developed side branches are. As a result, it controls the convexity of the crystal's envelope [see Fig. 14(c)]. For low values of L_{sat} ($L_{sat} = 1.0$), side branches are fully developed, and the envelope of the snowflake is weakly convex. Then, raising L_{sat} reduces the side branching instability and convexifies the snow crystal envelope. Noteworthy, when L_{sat} is close to 1, side branches overlap and form clusters. It is actually for $L_{sat} \sim 1.6$ that side branches are simultaneously developed and distinct.

2. Morphology diagram in experimentally accessible units

The morphology diagram in reduced units displayed in Fig. 13 can be transferred to real coordinates. It is represented in the experimental temperature-absolute humidity plane in Fig. 15 (colored domains). Experimental snowflakes from [8] are also spotted on the diagram (color marks).

The absolute humidity refers to the density excess over vapor-water equilibrium $\Delta\rho^W = \rho - \rho_{sat}^W$ (g m^{-3}), where ρ_{sat}^W is the vapor-water equilibrium density. First, the quantitative link between the reduced supersaturation u_0 used in our simulations and the density excess over vapor-water equilibrium $\Delta\rho^W$ is given by $u_0 = (\Delta\rho^W + \rho_{sat}^W - \rho_{sat}^I)/\rho_{sat}^I$, where ρ_{sat}^I is the vapor-ice equilibrium density. ρ_{sat}^W and ρ_{sat}^I are converted from tabulated saturation vapor pressures in the perfect gas framework, using $\rho_{sat}^{I,W} = C P_{sat}^{I,W}(T)/T$. Here, $C = 2.167$ g m^{-3} Pa^{-1} K (see Appendix). As a result, the reduced supersaturation u_0 is a function of both $\Delta\rho^W$ and
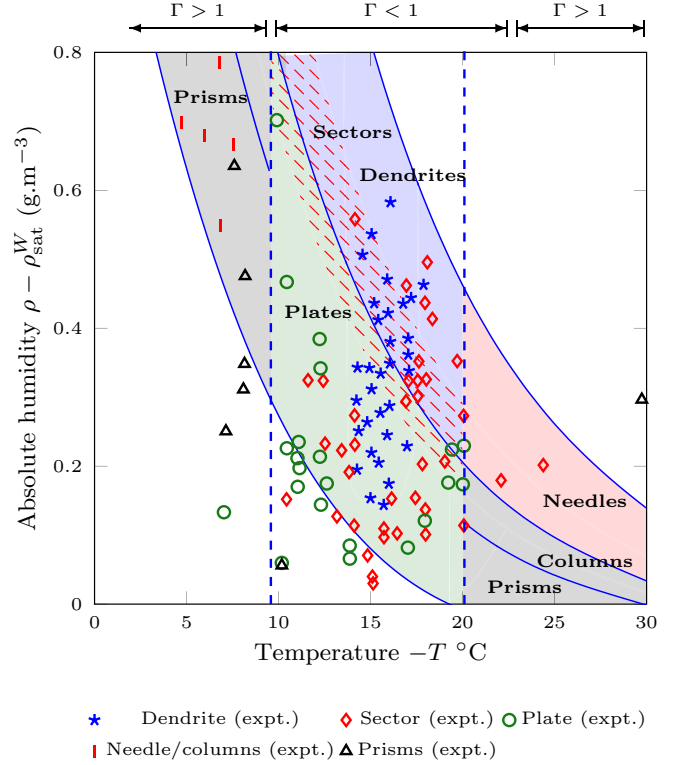

FIG. 15. T-ρ morphology diagram for snowflakes. The shapes of experimentally observed snowflakes are indicated by different marks, and the domains for the different morphologies obtained in PF simulations are shown by different colors.

T. Level sets of u_0 thus correspond to curves in the diagram. Second, the parameter Γ is related to the dimensionless attachment coefficient α^{kin}, encompassing the molecular kinetics at the solid-vapor interface [69]. The evolution of α^{kin} with the temperature was established in Ref. [69]. It notably accounts for the alternation of vertical and horizontal growth preference with the temperature. However, the physical interpretation of this dependence is still unclear [32]. In this work, the link between Γ and the temperature was simplified, as only two values of Γ were used: $\Gamma \sim 0.5$ for horizontal growth and $\Gamma = 3.0$ for vertical growth. This rough phenomenological setting of Γ reduces to $\Gamma < 1$ or $\Gamma > 1$, depending on the temperature.

This parametrization provided the morphology domains of simulated snowflakes on the diagram. Each domain is delimited by the intersection of vertical dashed lines in blue for $\Gamma < 1$ or $\Gamma > 1$ inversion, and blue lines for u_0 level sets. As a result, our simulation domains roughly cover experimental observations in the case of hexagonal plates (green circles) and columns (black triangles). The sector formation domain is also properly placed on the diagram, compared to experimental sector observations (red diamonds). However, the associated range of temperatures is too large, and the range of supersaturations is too narrow. The same shortcoming is observed for dendrites (blue stars). In addition to this, the numerical dendrite domain is shifted vertically by 0.15 g m^{-3} compared to observations. This disparity is amplified at high temperatures. Consequently, the simulated needle domain and the experimental needle spots do not overlap.

The global upward shift of the simulated morphology domains compared to observations shows that the u_0 values used in simulations were too high. This problem may be solved by rising the parameter λ, at the price of increased simulation resources. However, this discrepancy diverges when the temperature draws to 0. This suggests that the influence of the temperature on snowflake growth is more complex than an alternation between vertical and horizontal morphologies. First, the evolution of Γ with the temperature cannot be reduced to two domains defined by $\Gamma > 1$ or $\Gamma < 1$. It should be precisely fitted on α^{kin}. Besides, α^{kin} also depends on the supersaturation [69]. This additional dependence might explain the horseshoe shape of experimental plate formation in the diagram. Second, the dependence of L_{sat} on the temperature was neglected in this work, although it might play a significant role in the parametrization of the model. Indeed, this parameter is involved in the branching instability of ice crystals, which is notably responsible for the transition from prisms to needles. The parametrization of L_{sat} might hence allow to achieve needle growth for lower supersaturations. Besides, it may also explain the absence of dendritic morphologies close to the limit between horizontal and vertical growth ($T \simeq -9°$ and $-20°$). Finally, small vapor supersaturations $\rho_{\mathrm{sat}}^I < \rho < \rho_{\mathrm{sat}}^W$ are beyond reach of the model, except for very small temperatures. This limitation suggests our model is complementary to the model of Barrett *et al.* [19].

3. Characteristic size of snowflakes

When it is possible, the dimensionalization of a phase-field model consists in computing the space scale $W_0 = d_0\lambda/0.8839$. Here, $d_0 \simeq 2$ nm [32] is the capillary length of ice, and the coupling parameter λ embodies the the free energy barrier between vapor and solid phases, which is not known precisely. In this work, $\lambda = 3.0$ was treated as a numerical parameter, consistently with the standard phase-field approach for dendritic growth [27]. Hence, λ cannot be used to go back to W_0. For that reason, we propose an alternative parametrization of the space scale. Figure 6 shed light on similar growth stages for simulated and real snowflakes. Hence, if the real size of a particular simulated snowflake can be determined, we assume that the corresponding space scale W_0 can be transferred to other simulated snowflakes.

In our simulations, the hexagonal plate (bottom left of Fig. 13) reaches a stationary state. Besides, its shape is identical to the ECS of snowflakes observed by Colbeck *et al.* for $T = -15°$ in Ref. [40]. The size of this experimental hexagonal plate is 0.2 mm. Now, the size of the corresponding simulated plate is $40\Delta x = 32W_0$. This gives the following order of magnitude for the simulation space scale: $W_0 \sim 0.006$ mm. This approach provides consistent results with experiments [10,70] in Table I. We believe that this result is encouraging as for the capacity of the present model to predict the morphology and the size of snowflakes, depending on atmospheric conditions. Yet, one should keep in mind that the comparison between snowflake sizes is mostly qualitative, as most snow crystals do not reach a steady-state dimension. In Table I, the characteristic size of each snowflake shape was estimated at the first moment when the shape of the snowflake is definitive, so that further evolution consists of a scaling of this morphology.

TABLE I. Comparison of snowflake characteristic size between experiments on free falling snowflakes [10,70] and our parametrization based on a reference equilibrium snowflake (ref.) in Ref. [40].

Size						
Simu. (W_0)	32	24	130	64	120	640
Simu. (mm)	0.2 (ref.)	0.15	0.8	0.4	0.72	3.84
Expt. (mm)	0.2 (ref.)	0.1	1	0.5	0.4	4

IV. CONCLUSIONS

In this work, we addressed the challenging issue of snowflake growth simulation in three dimensions. It was demonstrated that the new phase-field method developed in Ref. [30] could provide an efficient, accurate, and predictive tool to investigate snowflake morphology and growth kinetics dependence on supersaturation and temperature. The most significant achievements are the following:

(i) The growth kinetics of snowflakes was simulated in three dimensions using the phase-field model.

(ii) The morphology of most experimentally observed snowflakes was faithfully reproduced.

(iii) The growth process was proved to embody the competition between surface tension and branching instability in the fast growth direction and terrace growth in the slow growth direction. In the slow growth direction, the formation of macrosteps was observed to reflect the main stages of snowflake growth history.

(iv) Ice crystal growth velocity was found to satisfy the solvability theory, consistently with former simulations and experiments on ice crystals.

(v) A morphology diagram for simulated snowflakes in reduced coordinates was connected to experimentally accessible units. The size of simulated snowflakes is in good agreement with experimental ones.

In the future, the present approach will be extended to pinpoint more subtle features of snowflake growth in atmosphere, such as the effects of air flows on the morphology. This model has thus vocation to merge the phase-field formulation with the equations of Navier-Stokes [71].

APPENDIX: SUPERSATURATION DIMENSIONALIZATION

The water vapor density ρ (g m^{-3}) is defined by

$$\rho = \frac{m}{V} = \frac{nM}{V} = \frac{M}{R} \times \frac{P}{T},$$

where m (g) is the mass of water in the volume V (m^3) of vapor, P (Pa) is the partial pressure of vapor, T (K) is the temperature of vapor, $M = 18.02$ g mol^{-1} is the molar mass of water, $R = 8.314$ m^3 Pa mol^{-1} K^{-1} is the ideal gas constant. Here, we used the ideal gas relation. This gives $\rho = CP/T$, where $C = M/R = 2.167$ m^{-3} g Pa^{-1} K. The relation remains the same for vapor-ice equilibrium density $\rho_{sat}^{I,W}$:

$$\rho_{sat}^{I,W} = C \frac{P_{sat}^{I,W}(T)}{T},$$

where the saturation vapor pressures above ice and water $P_{sat}^{I,W}(T)$ were tabulated in the literature. Besides, the reduced supersaturation u_0 is defined by $u_0 = (c - c_{sat}^{I})/c_{sat}^{I}$, where $c_{sat}^{I}(T)$ (m^{-3}) is the saturation number density of vapor above ice, at temperature T. Using that $\rho = m_{H_2O}c$, where m_{H_2O} is the mass of a molecule of water, u_0 can be written $u_0 = (\rho - \rho_{sat}^{I})/\rho_{sat}^{I}$. This provides the parametrization of the reduced supersaturation u_0, with respect to the density excess over vapor-water equilibrium $\Delta\rho^W$ and the temperature T:

$$u_0(\Delta\rho^W, T) = \frac{\Delta\rho^W + \rho_{sat}^W - \rho_{sat}^I}{\rho_{sat}^I}$$

$$= \frac{\Delta\rho^W + C P_{sat}^W(T)/T - C P_{sat}^I(T)/T}{C P_{sat}^I(T)/T}.$$

[1] P. Ball, Nat. Mater. **15**, 1060 (2016).

[2] I. A. Ryzhkin, Nat. Phys. **12**, 996 (2016).

[3] B. Pamuk, J. M. Soler, R. Ramírez, C. P. Herrero, P. W. Stephens, P. B. Allen, and M.-V. Fernández-Serra, Phys. Rev. Lett. **108**, 193003 (2012).

[4] E. Porcheron, P. Lemaitre, J. P. A. J. Van Beeck, R. Vetrano, M. Brunel, G. Grehan, and L. Guiraud, J. Eur. Opt. Soc. Rapid. Publ. **10**, 15030 (2015).

[5] J. J. Kielar, P. Lemaitre, C. Gobin, W. Yingchun, E. Porcheron, S. Coetmellec, G. Grehan, and M. Brunel, Opt. Commun. **372**, 185 (2016).

[6] U. Nakaya, I. Satô, and Y. Sekido, J. Faculty Sci., Hokkaido Imperial University. Ser. 2, Physics **2**, 1 (1938).

[7] U. Nakaya, *Compendium of Meteorology* (Springer, Berlin, 1951), pp. 207–220.

[8] J. S. Marshall and M. P. Langleben, J. Meteorol. **11**, 104 (1954).

[9] T. Kobayashi, Philos. Mag. **6**, 1363 (1961).

[10] C. Magono, W. Chung *et al.*, J. Faculty Sci., Hokkaido University. Ser. 7, Geophysics **2**, 321 (1966).

[11] K. G. Libbrecht, Annu. Rev. Mater. Res. **47**, 271 (2017).

[12] J. Nelson, Philos. Mag. A **81**, 2337 (2001).

[13] T. Kuroda and R. Lacmann, J. Cryst. Growth **56**, 189 (1982).

[14] J. Benet, P. Llombart, E. Sanz, and L. G. MacDowell, Phys. Rev. Lett. **117**, 096101 (2016).

[15] C. A. Reiter, Chaos Solitons Fract. **23**, 1111 (2005).

[16] J. Gravner and D. Griffeath, Phys. Rev. E **79**, 011601 (2009).

[17] J. G. Kelly and E. C. Boyer, Cryst. Growth Des. **14**, 1392 (2014).

[18] J. Li and L. P. Schaposnik, Phys. Rev. E **93**, 023302 (2016).

[19] J. W. Barrett, H. Garcke, and R. Nürnberg, Phys. Rev. E **86**, 011604 (2012).

[20] K. G. Libbrecht, *Ken Libbrecht's Field Guide to Snowflakes* (Voyageur Press, St. Paul, MN, 2006).

[21] G. Sazaki, S. Zepeda, S. Nakatsubo, E. Yokoyama, and Y. Furukawa, Proc. Natl. Acad. Sci. USA **107**, 19702 (2010).

[22] W. Shimada and K. Ohtake, Cryst. Growth Des. **16**, 5603 (2016).

[23] K. Kikuchi and H. Uyeda, Atmos. Res. **4748**, 169 (1998).

[24] I. Singer-Loginova and H. M. Singer, Rep. Prog. Phys. **71**, 106501 (2008).

[25] A. Karma and W.-J. Rappel, Phys. Rev. E **53**, R3017 (1996).

[26] A. Karma, Phys. Rev. Lett. **87**, 115701 (2001).

[27] J. C. Ramirez, C. Beckermann, A. Karma, and H. J. Diepers, Phys. Rev. E **69**, 051607 (2004).

[28] A. Cartalade, A. Younsi, and M. Plapp, Comput. Math. Appl. **71**, 1784 (2016).

[29] J. W. Barrett, H. Garcke, and R. Nürnberg, IMA J. Numer. Anal. **34**, 1289 (2013).

[30] G. Demange, H. Zapolsky, R. Patte, and M. Brunel, npj Comput. Mater. **3**, 1 (2017).

[31] A. J. Meuler, J. D. Smith, K. K. Varanasi, J. M. Mabry, G. H. McKinley, and R. E. Cohen, ACS Appl. Mater. Interfaces **2**, 3100 (2010).

[32] K. G. Libbrecht, Rep. Prog. Phys. **68**, 855 (2005).

[33] T. Uehara and R. F. Sekerka, J. Cryst. Growth **254**, 251 (2003).

[34] M. Fleck, L. Mushongera, D. Pilipenko, K. Ankit, and H. Emmerich, Eur. Phys. J. Plus **126**, 95 (2011).

[35] J. J. Eggleston, G. B. McFadden, and P. W. Voorhees, Phys. D (Amsterdam) **150**, 91 (2001).

[36] S. G. Kim and W. T. Kim, J. Cryst. Growth **275**, e355 (2005).

[37] G. B. McFadden, A. A. Wheeler, R. J. Braun, S. R. Coriell, and R. F. Sekerka, Phys. Rev. E **48**, 2016 (1993).

[38] R. F. Sekerka, J. Cryst. Growth **275**, 77 (2005).

[39] F. Liu and J. Shen, Math. Methods Appl. Sci **38**, 4564 (2015).

[40] S. C. Colbeck, J. Cryst. Growth **72**, 726 (1985).

[41] W. F. Berg, Proc. R. Soc. A **164**, 79 (1938).

[42] K. Iwai, Atmos. Res. **24**, 137 (1989).

[43] T. Gonda and S. Nakahara, J. Cryst. Growth **173**, 189 (1997).

[44] J. Langer and H. Müller-Krumbhaar, Acta Metall. **26**, 1681 (1978).

[45] K. G. Libbrecht (private communication).

[46] K. G. Libbrecht, Snowcrystals.com, http://www.snowcrystals.com.

[47] J. Nelson, Cryst. Growth Des. **5**, 1509 (2005).

[48] P. R. Field and A. J. Heymsfield, J. Atmos. Sci. **60**, 544 (2003).

[49] A. Younsi and A. Cartalade, J. Comput. Phys. **325**, 1 (2016).

[50] G. P. Ivantsov, Dokl. Akad. Nauk SSSR **58**, 567 (1947) [English translation in P. Pelcé, *Dynamics of Curved Fronts* (Academic Press, New York, 1988)].

[51] D. V. Alexandrov and P. K. Galenko, J. Phys. Chem. Solids **108**, 98 (2017).

[52] G. Horvay and J. Cahn, Acta Metall. **9**, 695 (1961).

[53] K. G. Libbrecht, T. Crosby, and M. Swanson, J. Cryst. Growth **240**, 241 (2002).

[54] E. Brener and V. Melnikov, Zh. Eksp. Teor. Fiz. **107**, 628 (1995) [J. Exp. Theor. Phys. **80**, 341 (1995)].

[55] P. Pelcé and D. Bensimon, Nucl. Phys. B, Proc. Suppl. **2**, 259 (1987).

[56] P. Pelcé and A. Libchaber, *Dynamics of Curved Fronts* (Elsevier, Amsterdam, 2012).

[57] E. Brener, J. Cryst. Growth **99**, 165 (1990).

[58] E. Brener and V. Mel'Nikov, Adv. Phys. **40**, 53 (1991).

[59] K. G. Libbrecht and V. M. Tanusheva, Phys. Rev. E **59**, 3253 (1999).

[60] K. Libbrecht, J. Cryst. Growth **247**, 530 (2003).

[61] D. A. Kessler, J. Koplik, and H. Levine, Adv. Phys. **37**, 255 (1988).

[62] M. B. Amar and E. Brener, Phys. Rev. Lett. **71**, 589 (1993).

[63] E. A. Brener, J. Cryst. Growth **166**, 339 (1996).

[64] D. V. Alexandrov and P. K. Galenko, Phys. Rev. E **87**, 062403 (2013).

[65] D. Alexandrov, D. Danilov, and P. Galenko, Int. J. Heat Mass Transfer **101**, 789 (2016).

[66] A. Barbieri and J. S. Langer, Phys. Rev. A **39**, 5314 (1989).

[67] C. Misbah, J. Phys. **48**, 1265 (1987).

[68] Y. Saito, G. Goldbeck-Wood, and H. Müller-Krumbhaar, Phys. Rev. Lett. **58**, 1541 (1987).

[69] K. G. Libbrecht and M. E. Rickerby, J. Cryst. Growth **377**, 1 (2013).

[70] T. Takahashi, T. Endoh, G. Wakahama, and N. Fukuta, J. Meteorol. Soc. Jpn. Ser. II **69**, 15 (1991).

[71] R. Rojas, T. Takaki, and M. Ohno, J. Comput. Phys. **298**, 29 (2015).